

Supporting Information

Real-Time Capture of Nuclear Motions Influencing Photoinduced Electron Transfer

Pyosang Kim,^{*,1,2} Subhangi Roy,³ Andrew J. S. Valentine,⁴ Xiaolin Liu,⁴ Sarah Kromer,³ Tae Wu Kim,¹ Xiaosong Li,^{*,4} Felix N. Castellano^{*,3} and Lin X. Chen^{*,1,2}

¹Chemical Sciences and Engineering Division, Argonne National Laboratory, Lemont, IL 60439

²Chemistry Department, Northwestern University, Evanston, IL 60208

³Chemistry Department, North Carolina State University, Raleigh, NC 27695-8204

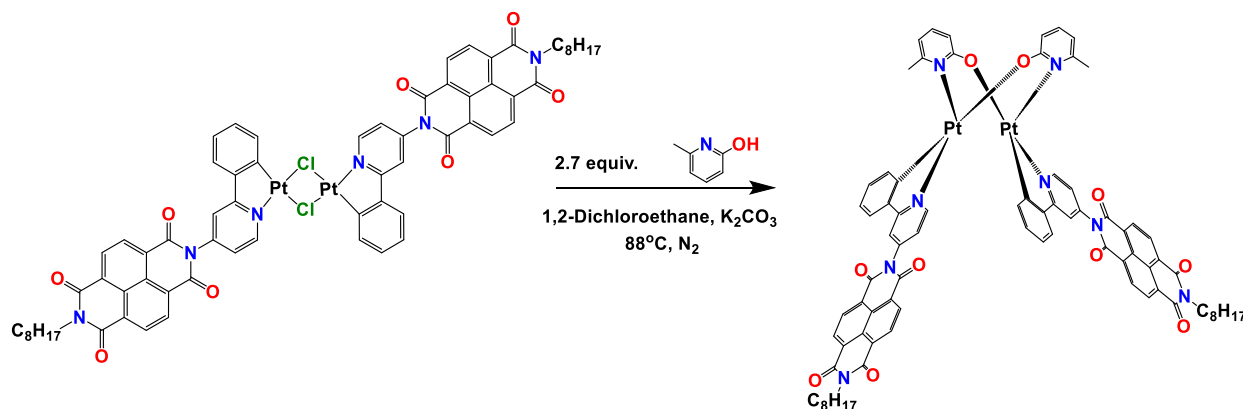
⁴Chemistry Department, University of Washington, Seattle, WA 98195

Experimental Section.

Sample Preparation. All starting materials were purchased from Fisher Scientific, Sigma-Aldrich, or VWR, and used as received. NDIPpy,^{1, 2} all Pt-containing intermediates ([Pt(DMSO)₂Cl₂], [Pt(ppy)(μ-Cl)]₂, and [Pt(NDIPpy)(μ-Cl)]₂),³⁻⁵ and [Pt(ppy)(6-Me-2-hydroxypyridine)]₂ (**1**),⁴ were prepared according to methods previously described in the literature.

[Pt(NDIPpy)(6-Me-2-hydroxypyridine)]₂ (**2**) was synthesized by the following modified procedure.^{4, 5} [Pt(NDIPpy)(μ-Cl)]₂ (0.402 g, 0.264 mmol, 1 equiv.) and 6-methyl-2-hydroxypyridine (0.079 g, 0.723 mmol, 2.7 equiv.) were dissolved in 30 mL of 1,2-dichloroethane in the presence of excess K₂CO₃ (0.469 g, 3.39 mmol, 12.9 equiv.). Reflux proceeded at 88°C for 24 hours under N₂. At reaction completion, the mixture was cooled to room temperature and subsequently filtered to remove solid K₂CO₃. The filtrate was evaporated to dryness by rotary evaporation, then passed through a short alumina plug using CH₂Cl₂ as the eluent. The final dimer complex was collected as a red-colored band and evaporated to dryness. The isolated deep red solid was washed several times with hot MeCN and was then collected by vacuum filtration (0.120 g, 27.2% yield). ¹H NMR (400 MHz, CD₂Cl₂; ppm): 8.67 (quart., J = 7.9 Hz, 8H), 8.47 (d, J = 6.2 Hz, 2H), 7.63 (d, J = 2.1 Hz, 2H), 7.36-7.31 (m, 2H), 7.28 (dd, J = 8.5 Hz, 7.1 Hz, 2H), 6.82 (t, J = 3.9 Hz, 4H), 6.50 (d, J = 8.41, 2H), 6.40 (d, J = 6.8 Hz, 2H), 6.32 (dd, J = 6.1 Hz, 2.21 Hz, 2H), 6.28-6.22 (m, 2H), 4.18 (t, J = 7.6 Hz, 4H), 2.84 (s, 6H), 1.74 (quint., J = 7.1, 4H), 1.49-1.27 (m, 20H), 0.93-0.85 (m, 6H). ¹³C{¹H} NMR (700 MHz, CD₂Cl₂; ppm): 173.2, 167.7, 163.0, 162.2, 156.6, 150.6, 144.3, 143.7, 138.8, 138.5, 131.7, 131.5, 131.1, 130.1, 127.7, 127.4, 127.3, 126.7, 125.3, 122.1, 120.6, 119.7, 114.0, 110.5, 41.4, 32.2, 29.7, 29.6, 28.4, 27.5, 27.0, 23.1, 14.3. MALDI-TOF MS (C₇₈H₆₈N₈O₁₀Pt₂⁺) calc.: m/z = 1666.4354; found: m/z = 1666.4325.

Synthetic Schematic:



Proton NMR:

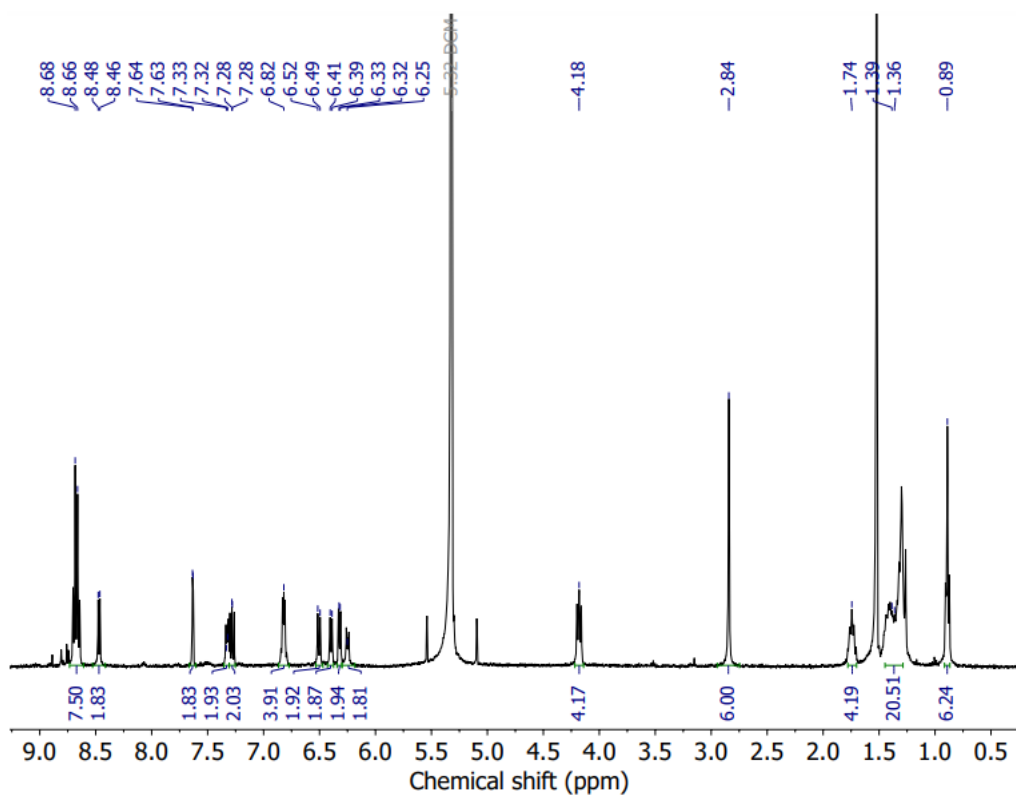


Figure S1. ¹H NMR spectrum of **2** (400 MHz, CD₂Cl₂).

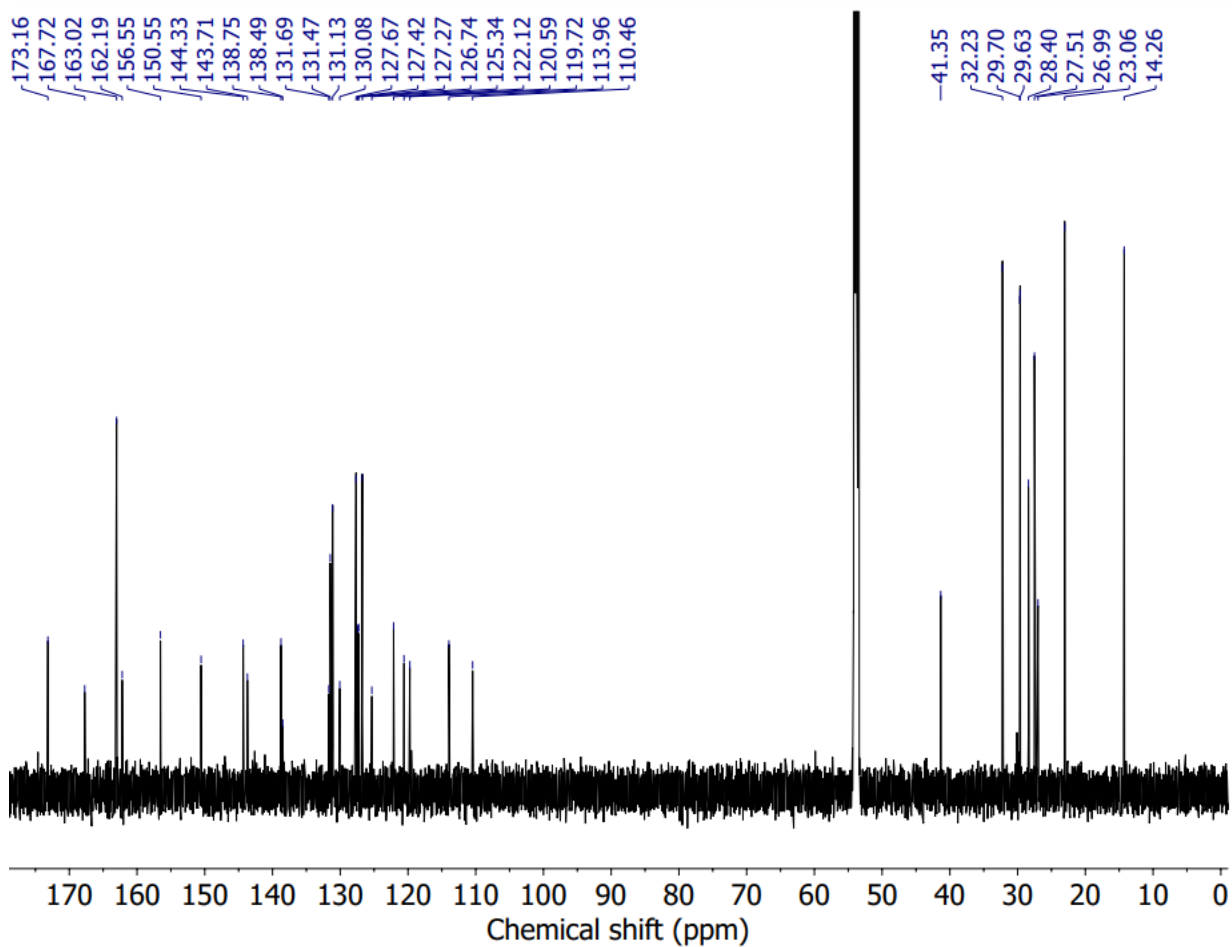


Figure S2. $^{13}\text{C}\{^1\text{H}\}$ NMR spectrum of **2** (700 MHz, CD_2Cl_2).

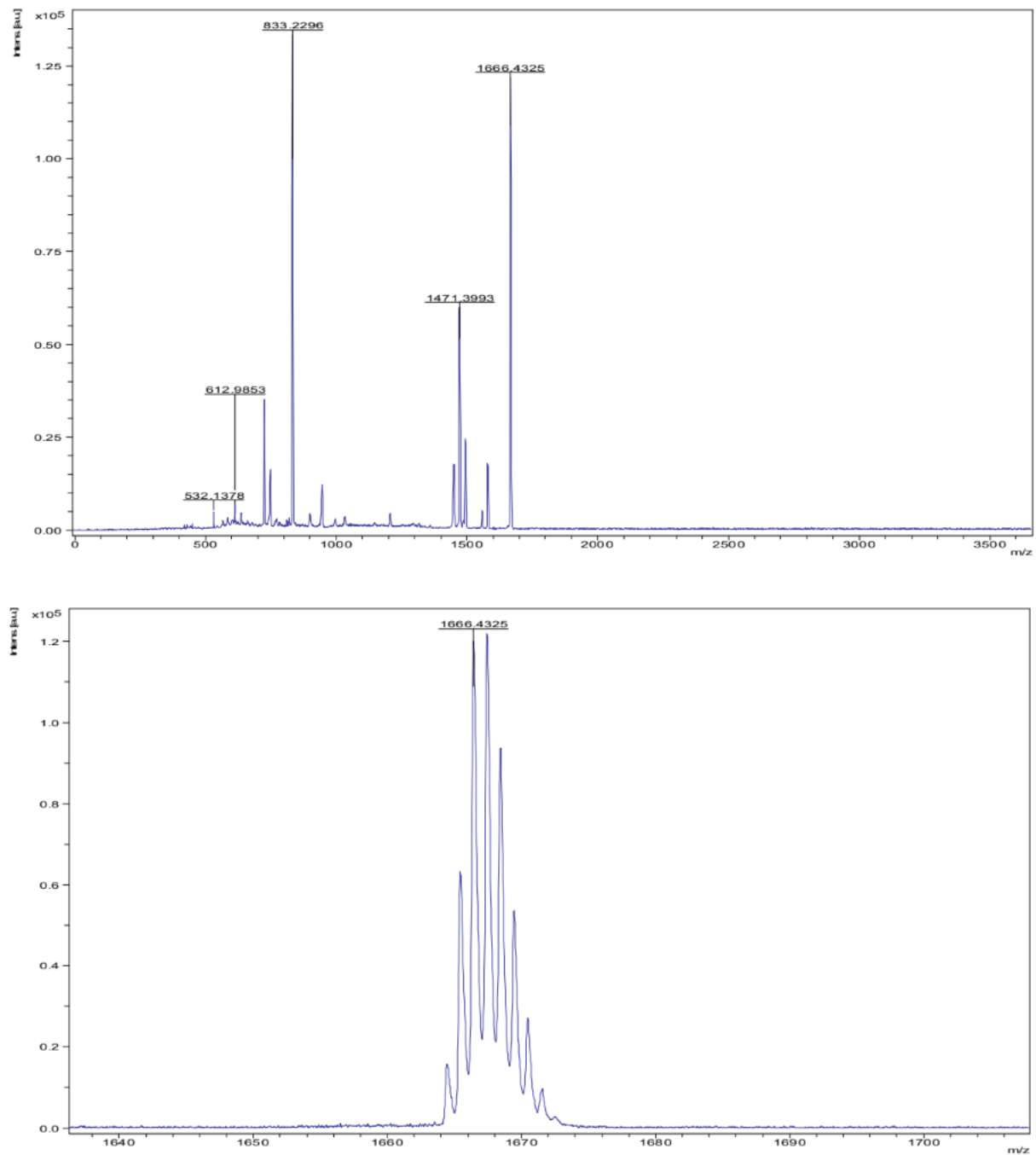


Figure S3. MALDI-TOF mass spectrum of **2**, (top) full mass spectrum, (bottom) zoomed in to M^+ .

Steady-State Measurements. Steady-state absorption spectra were measured at room temperature by Shimadzu UV-3600 UV-Vis-NIR spectrophotometer. Toluene, tetrahydrofuran (THF) and acetonitrile (MeCN) were purchased from Sigma-Aldrich and used without further purification.

Femtosecond Broadband Transient Absorption Spectroscopy. For the fs-BBTA measurements, a Yb:KGW regenerative amplifier (Light Conversion, Pharos-10W) was used to generate 1030 nm fundamental pulses at 10 kHz repetition rate with a pulse width of 160 fs. The fundamental beam was split in two pulses using 90/10 beam splitter to produce a visible pump and a broadband probe pulse. The high-power beams pumped a home-built noncollinear optical parametric amplifier (NOPA) to generate the pump pulses centered at ~ 545 nm with 55 nm bandwidth.⁶ The pump pulses were compressed with a chirped mirror pair (Laser Quantum, DCM-12) and a fused silica wedge pair (Newport) to the pulse duration of 19.9 fs at the sample position, which was characterized by a second-harmonic generation frequency-resolved optical gating (SHG-FROG) with a 5 μm thick Beta Barium Borate (BBO) crystal (United Crystals Inc.)

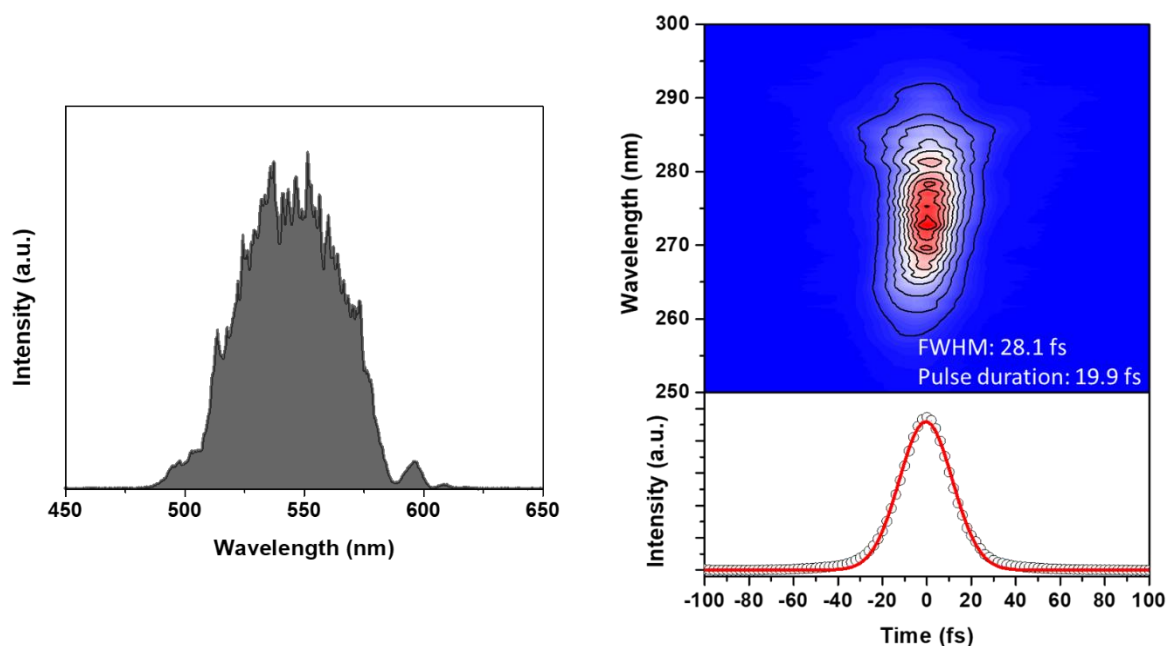


Figure S4. (Right) Pump laser pulse used for fs-BBTA measurements, and (left) the spectral and temporal profiles of the pump laser pulse obtained by the second-harmonic generation frequency-resolved optical gating (SHG-FROG). The pulse duration of 19.9 fs was characterized by fitting to a Gaussian function (red line) with 28.1 fs FWHM.

(Figure S4). For broadband probe, the low-power beams were focused on a 3 mm thick YAG window (EKSM) by a 10 cm plano-convex lens to generate white light continuum (WLC) covering 520 – 850 nm range. The WLC was subsequently compressed by a chirped mirror pair

(Laser Quantum, DCM-9). The pump and probe beams were focused on the sample contained in a 1 mm pathlength quartz cuvette using a 25 cm concave mirror. The optical time delay between pump and probe pulses was controlled by a motorized linear stage (Newport, XMS160-S). To measure the TA spectra, the “pump-on” and “pump-off” probe spectra were obtained by a chopper operating at 500 Hz and detected with a spectrometer (Andor, Kymera 328i) and a sCMOS camera (Andor, Zyla-5.5). The TA measurements were carried out with the pump polarization in a magic angle (54.7°) with respect to the probe polarization to prevent polarization-dependent signals. 1 mm pathlength quartz cuvettes (Starna Cells Inc.) were used for the TA measurements.

Quantum Mechanical Calculations. All calculations were performed at the University of Washington using GAUSSIAN16.⁷ We used the ω B97X-D functional⁴ with the LanL2DZ effective core potential (ECP) and corresponding basis set⁸ on Pt atoms and 6-31G(d) on light atoms for geometry optimization and UV-vis spectra calculations. This functional was chosen because it is range-separated, to better describe charge-transfer excited states,⁹ and it contains dispersion corrections, necessary to capture π - π interactions.¹⁰ Excited states were evaluated using linear response time-dependent density functional theory (TD-DFT). Energetic minima found by ground- and excited-state geometry optimizations were confirmed by normal mode calculations at the same level of theory.

Calculated Electronic Transitions.

To further characterize the lowest electronic transition, we carried out TD-DFT and natural transition orbital¹¹ (NTO) calculations. A slight red-shift of the MMLCT band maxima from 508 to 520 nm was caused by the covalent attachment of NDIs to cyclometalating phenylpyridine (ppy) ligands (Figure 1b). Based on the energy-minimized ground-state structures, a similar redshift in the optically allowed lowest transitions was reproduced in the calculations (Figure S5). NTO analysis was performed to visualize the lowest energy transitions with significant oscillator strengths (Figure S6). Both transitions show that the hole is localized on the $d\sigma^*$ orbital of the Pt(II) metals and the particle is localized on the π^* orbital of the ppy ligands. This result confirms that the lowest absorption bands for **1** and **2** originate from MMLCT transitions. It is noteworthy that a partial electronic delocalization between the ppy and NDI was found in the lowest unoccupied molecular orbital (LUMO)+2 and LUMO+4 which largely contribute to the MMLCT excitation (Figure S7). These MOs suggest that the redshift in the MMLCT band is attributed to the partial π -conjugation between the ppy ligands and NDIs.

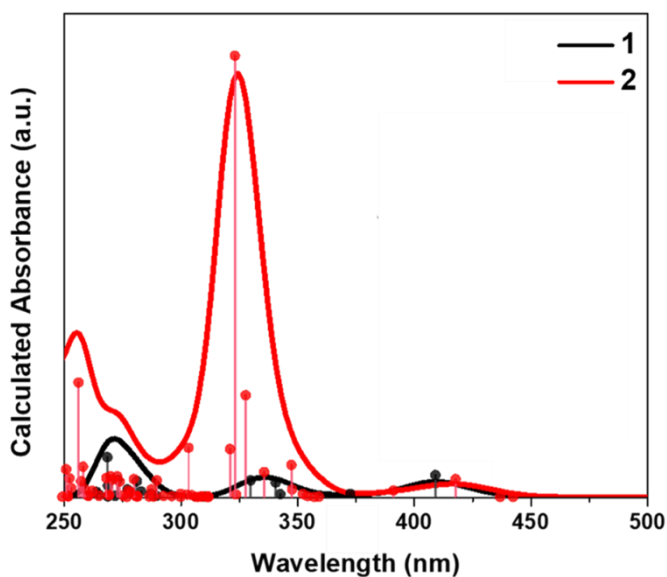


Figure S5. Calculated electronic transitions for **1** (black) and **2** (red). The spectra were generated by applying a 2000 cm^{-1} bandwidth to each transition using GaussSum 3.0.

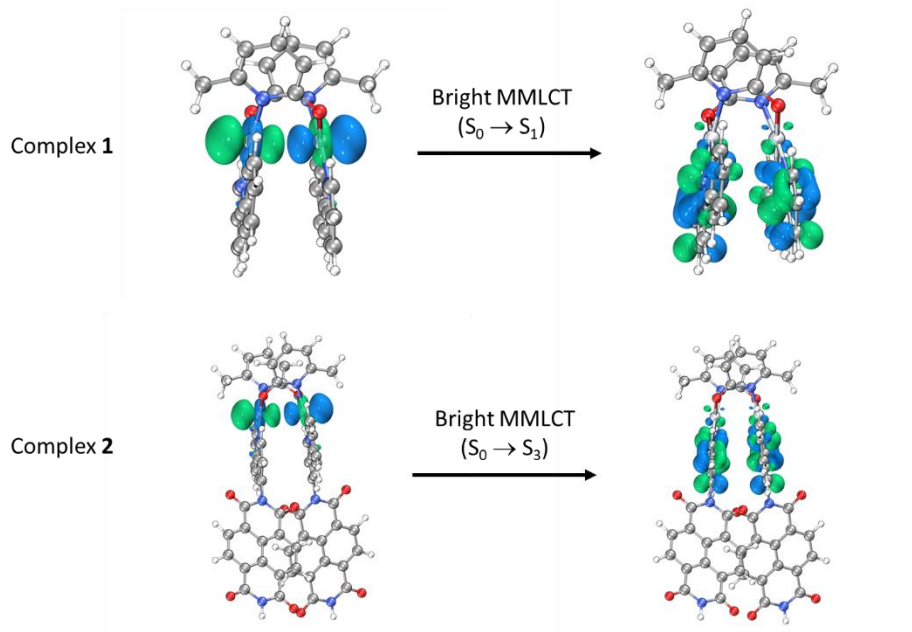


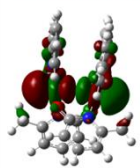
Figure S6. Natural transition orbitals for the lowest optically allowed transitions of **1** and **2**.

Table S1. Calculated Transition Wavelength, Oscillator Strength and Major Contributions for Electronic Transitions in Complexes **1** and **2**

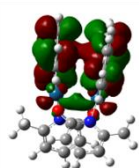
Sample	Wavelength (nm)	Oscillator Strength	Major Contributions ^a
Complex 1	409 ($S_0 \rightarrow S_1$)	0.0385	H→L (94%)
Complex 2	442 ($S_0 \rightarrow S_1$)	0	H→L (97%)
	436 ($S_0 \rightarrow S_2$)	0	H→L+1 (97%)
	417 ($S_0 \rightarrow S_3$)	0.0313	H→L+2 (29%), H→L+4 (65%)

^aPercentage contribution of the configuration is given in parenthesis. H and L mean HOMO and LUMO, respectively

Complex 1

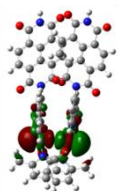


HOMO

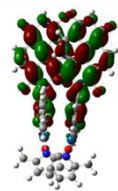


LUMO

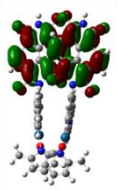
Complex 2



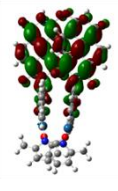
HOMO



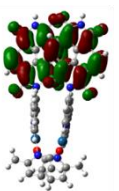
LUMO+2



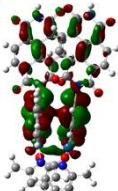
LUMO



LUMO+3



LUMO+1



LUMO+4

Figure S7. Molecular Orbitals contributing to $S_0 \rightarrow S_1$ for **1** and $S_0 \rightarrow S_1, S_2, S_3$ for **2**.

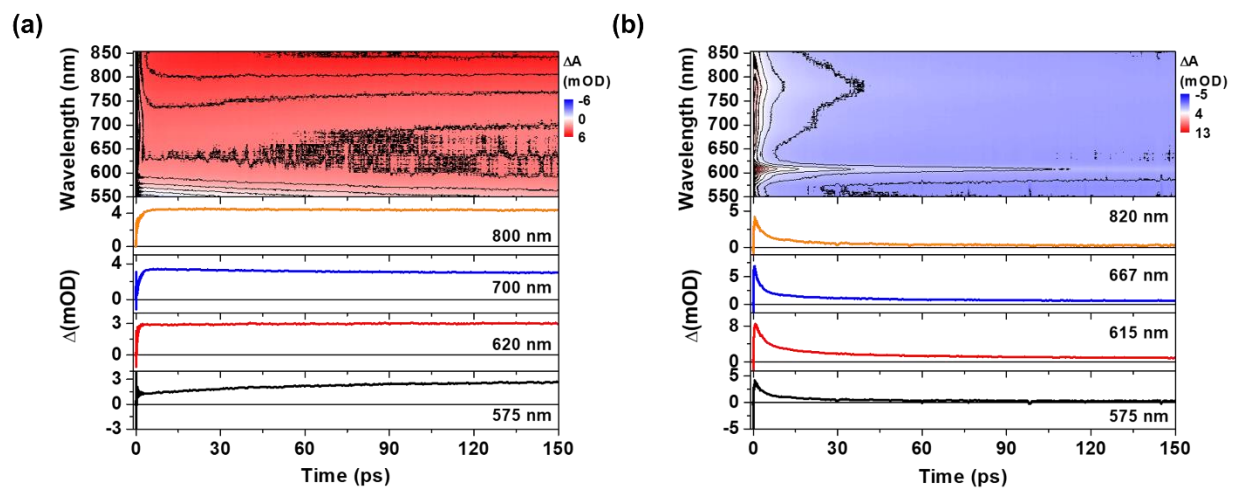


Figure S8. 2D contour plots of BBTA spectra and kinetic profiles up to 150 ps for **1** (a) and **2** (b)

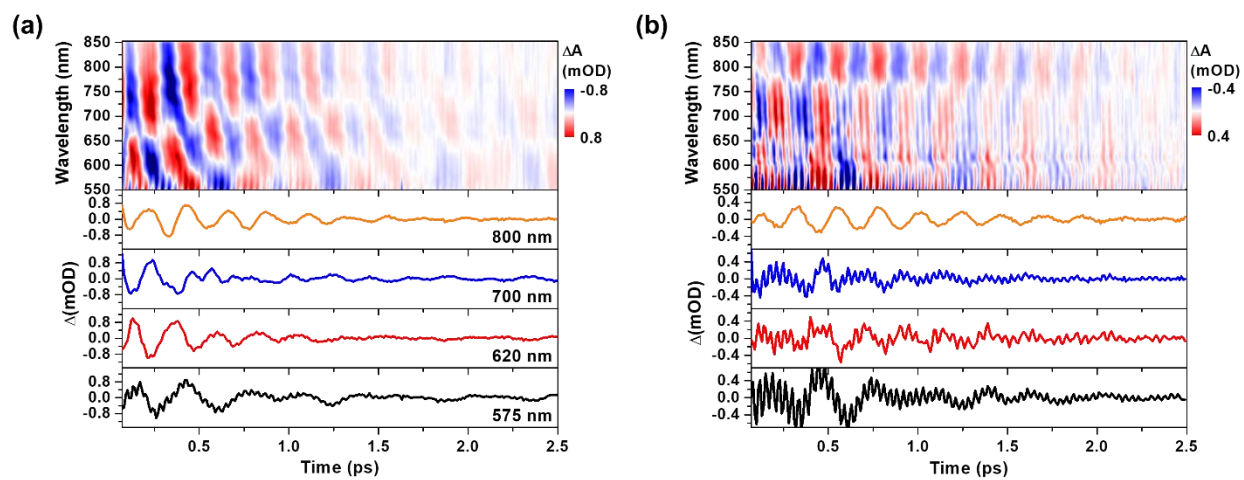


Figure S9. Oscillatory residuals for **1** (a) and **2** (b) without inverse Fourier filtering.

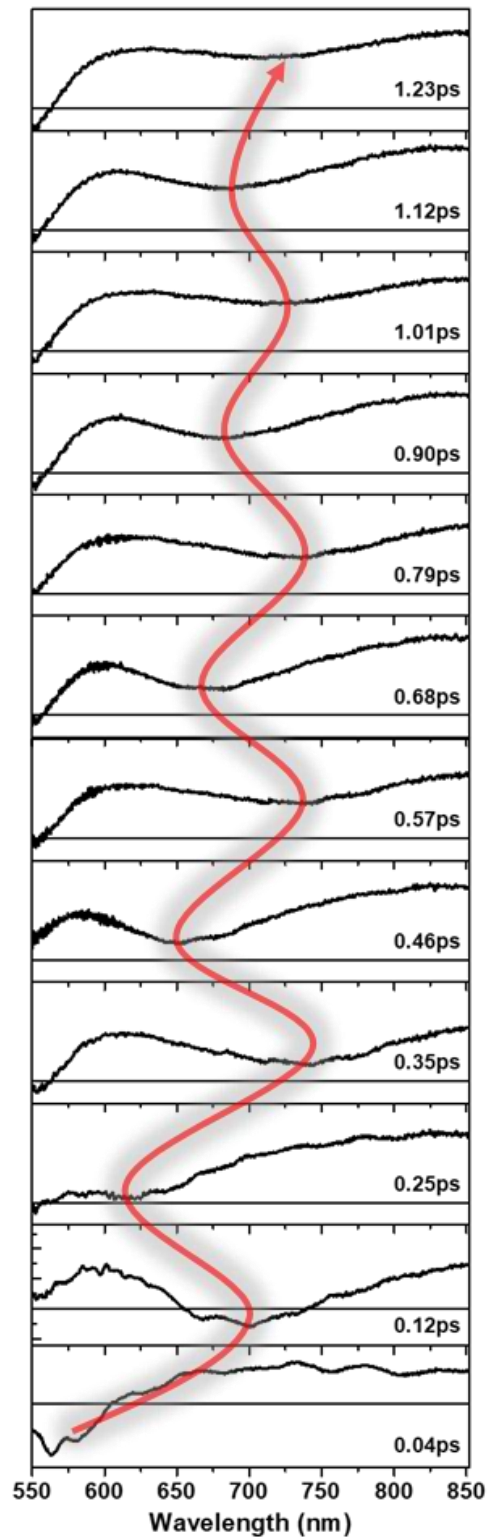


Figure S10. BBT spectra of which detected with a time interval of ~ 110 fs corresponding to half the period of 150 cm^{-1} CWP motion. Red arrow highlights the oscillatory motion of stimulated emission peak.

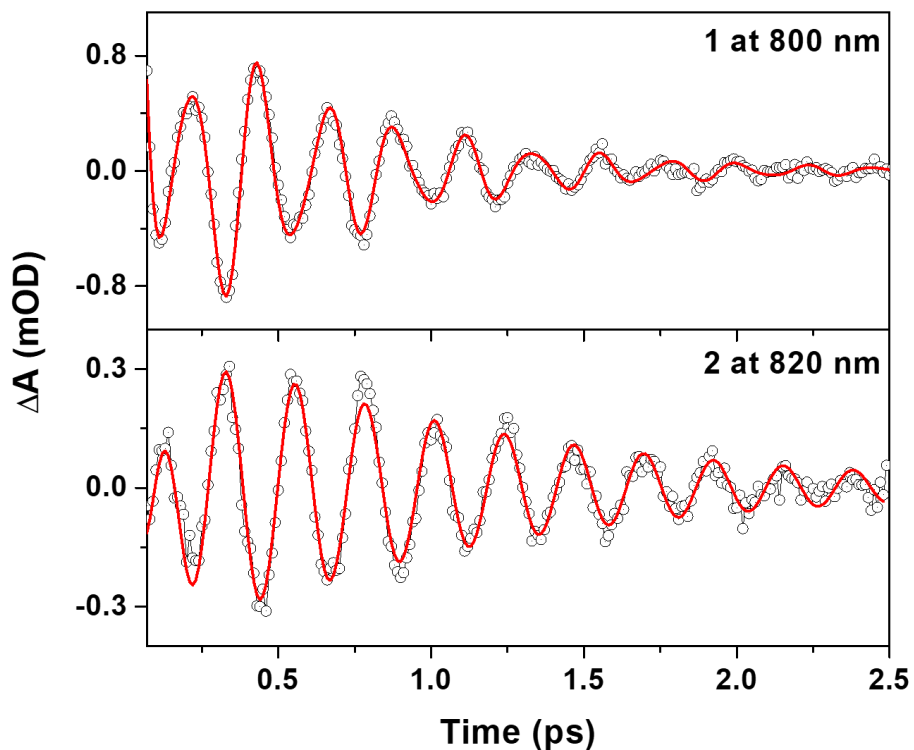


Figure S11. Beating signals obtained at 800 nm for **1** and 820 nm for **2**. These probe wavelengths exhibit 150 cm^{-1} CWP motions that are relatively less influenced by other CWP motions, making the region more suitable for determining the dephasing time of the Pt-Pt stretching motion. Red curve shows the fitting result by a combination of damped sine functions, $f(t) = \sum_i A_i e^{(-t/\tau_i)} \sin(2\pi t/T_i t + \varphi_i)$ where A is an oscillation amplitude scaling constant, τ = dephasing time, T = period, and φ = phase shift. The Fit results are listed in Table S2.

Table S2. Dephasing Time Constants for Beating Signals at 800 nm for **1** and 820 nm for **2**.

Parameter	1 at 800nm	2 at 820 nm
τ_1	$613 \pm 18\text{ fs}$ (150 cm^{-1})	$100 \pm 10\text{ fs}$ (rise, 150 cm^{-1})
τ_2	$646 \pm 77\text{ fs}$ (230 cm^{-1})	$1.0 \pm 0.05\text{ ps}$ (decay, 150 cm^{-1})

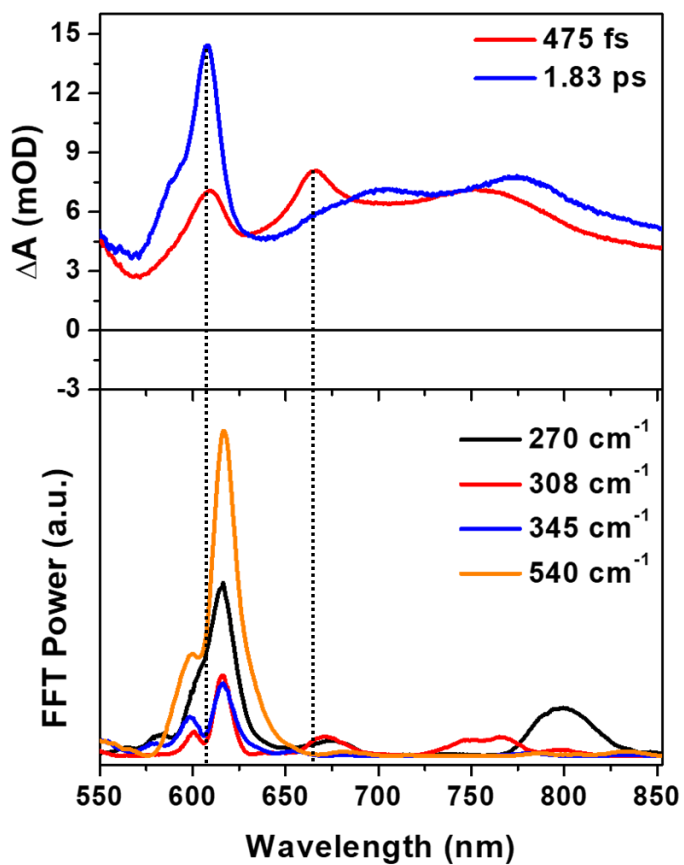


Figure S12. FFT amplitude distribution plots for the 270, 308, 345 and 540 cm^{-1} modes as a function of probe wavelength. EADSs with the time constants of 475 fs (red) and 1.83 ps (blue) are presented to compare the spectra of intermediate and CS states with FFT amplitude distribution.

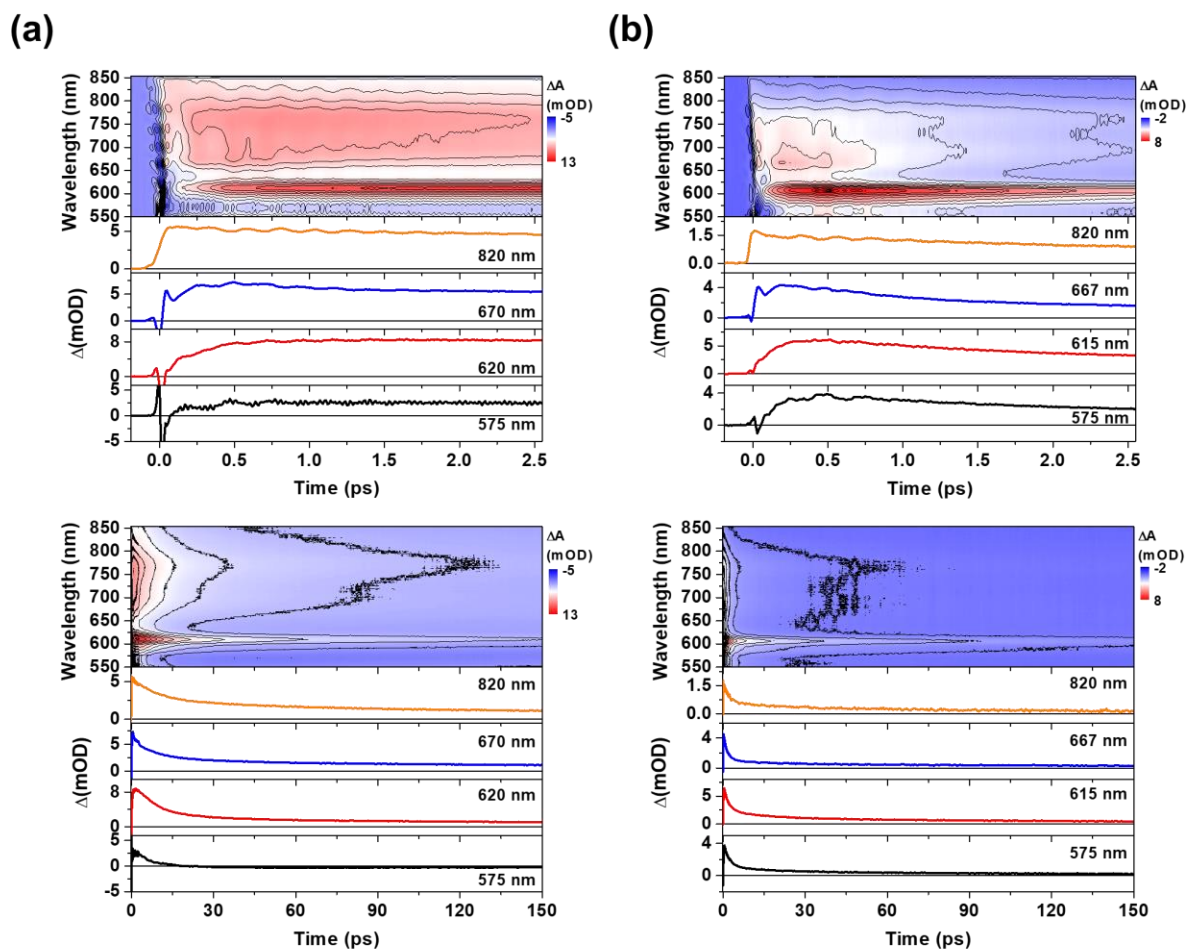


Figure S13. (a and b) 2D contour plots of BBTA spectra and kinetic profiles for **2** in toluene (a) and MeCN (b), scanned up to 2.5 ps (top) and 150 ps (bottom)

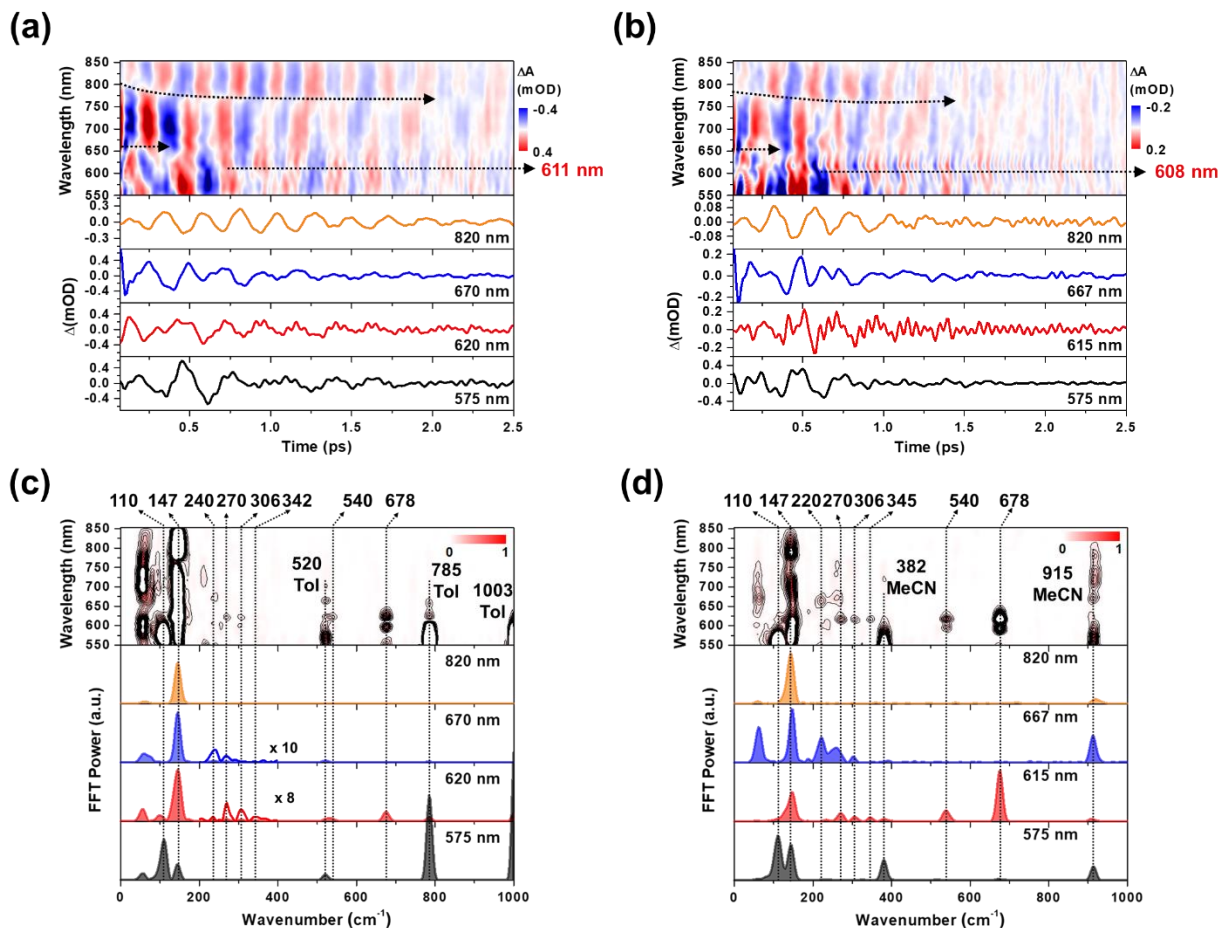


Figure S14. (a and b) wavelength-resolved residual map (top) and beating signals (bottom) for complex **2** in toluene (a) and MeCN (b). The oscillatory residuals were extracted by a global kinetic analysis on the BBTA kinetic traces. We performed inverse Fourier filtering on the CWP modes in 0-700 cm^{-1} in order to visualize the temporal dynamics of the CWP motions obscured by strong solvent vibrations at 785, 1003 cm^{-1} for toluene and 915 cm^{-1} for MeCN. (c and d) wavelength-resolved FFT map (top) and spectra (bottom) at specific probe wavelengths for complex **2** in toluene (c) and MeCN (d). The FFT was carried out for the residuals within the time range of 0.07 – 2.5 ps to avoid the contribution of cross-phase modulation around time zero.

Short-Time Fourier Transformation Analysis.

Using short-time Fourier transformation (STFT) method, we analyze the temporal evolution of CWP motions and their correlation with the PET kinetics. The STFT divides the time evolution of the oscillatory signals in the experimental delay time window into shorter overlapping segments and then performs the FT on each segment. Thus, the results from this procedure enable us to extract the time evolution of the amplitude and frequency of various vibrational modes. Specifically, an FT window of 800 fs was used for the STFT and slid with a 100-fs time step over the delay time range from 0.07 to 1.67 ps, as depicted in Figure S11.

STFT Procedure

1. Window Slicing

Slice signal into overlapping windows with the size of 800 fs

2. Windowing

Apply windowing function (Kaiser, $\beta = 4$)

3. Zero Padding

Zero pad to increase spectral resolution

4. Fast Fourier Transform

Convert to frequency domain

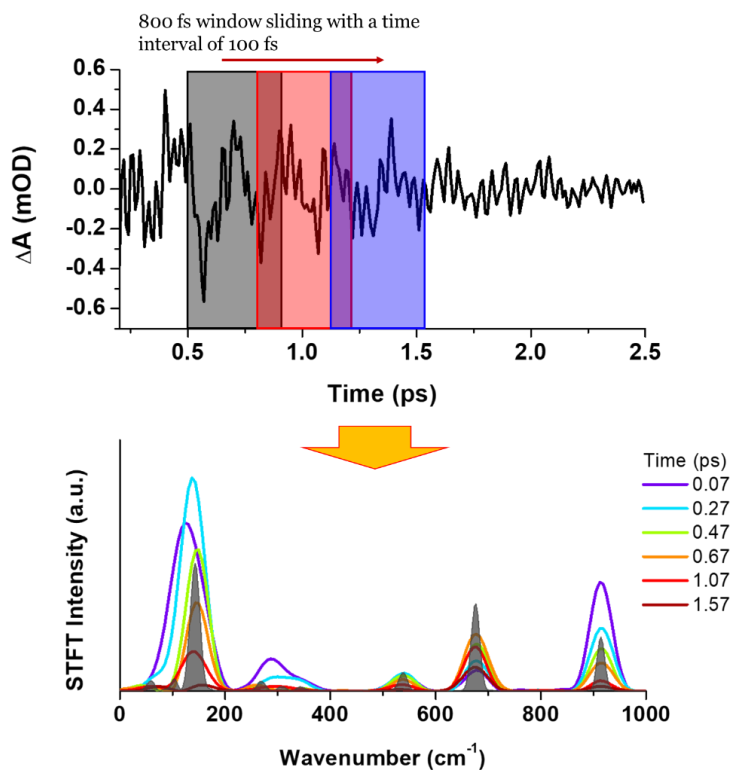


Figure S15. STFT procedure and exemplary STFT spectra obtained from the beating signals at 615 nm for complex 1.

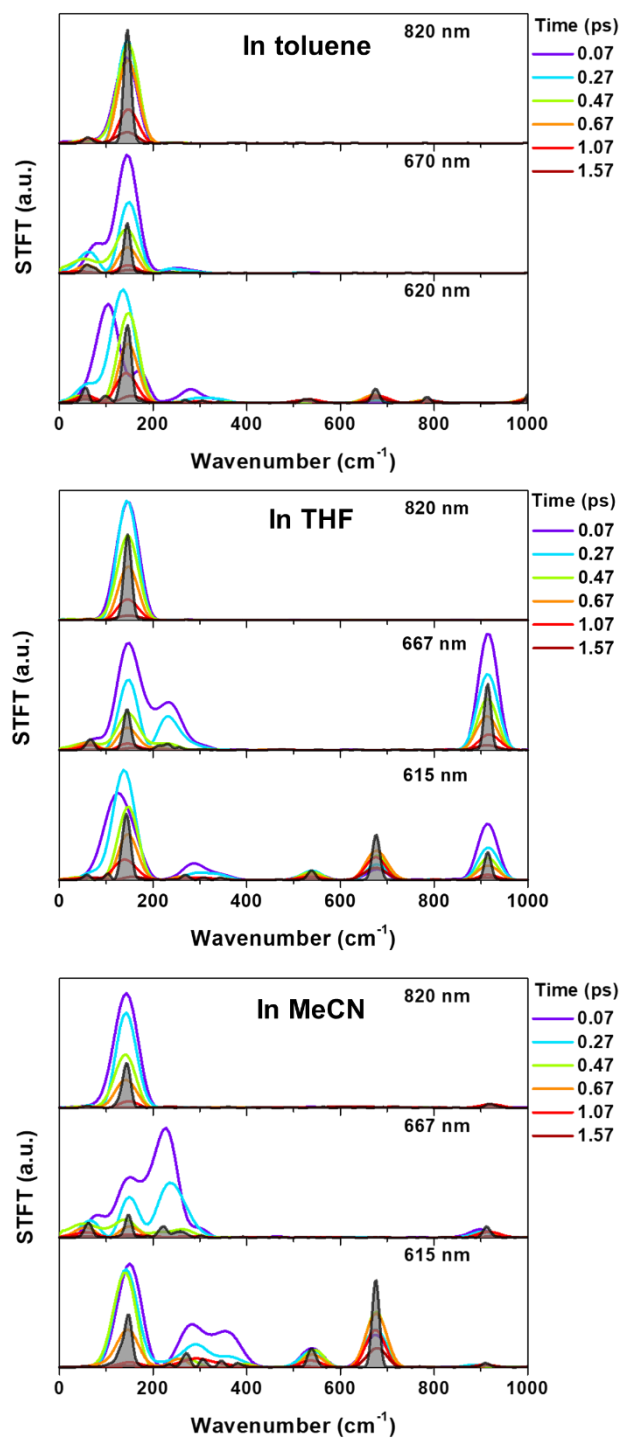


Figure S16. STFT spectra of beating signals detected at ~ 615 , ~ 667 and 820 nm in toluene (top), THF (middle) and MeCN (bottom). The spectra filled in gray represent the FFT spectra of the same oscillations across entire pump-probe delay.

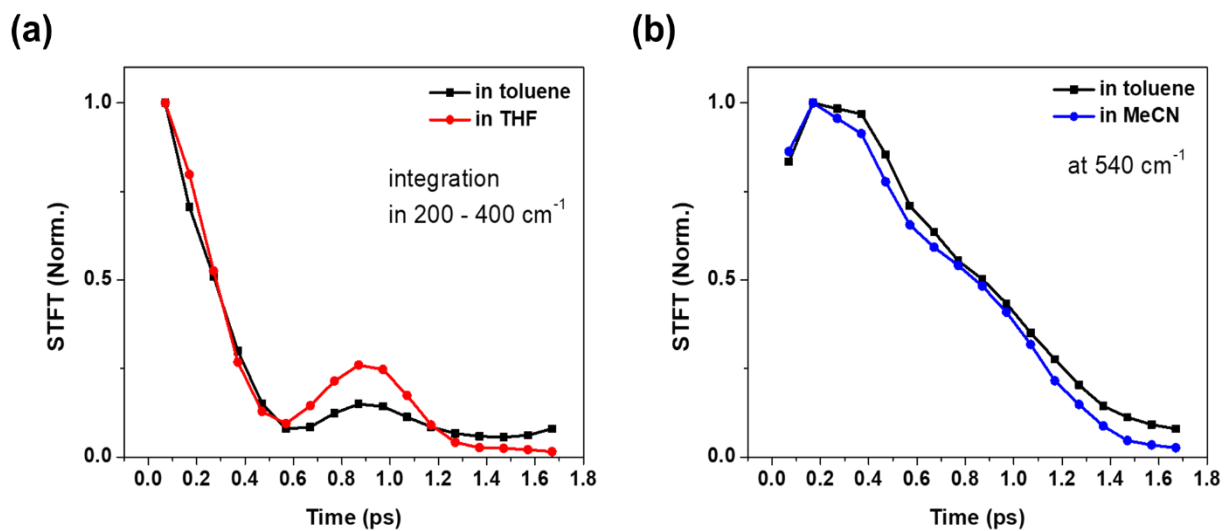
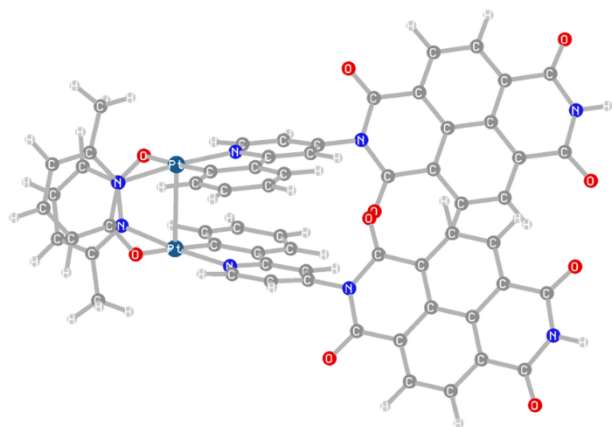


Figure S17. Time traces of STFT amplitudes: (a) 270, 308 and 345 cm^{-1} modes observed at ~ 615 nm; the STFT amplitudes at each time points were integrated in the frequency range of 200 – 300 cm^{-1} . (b) 540 cm^{-1} mode observed at 615 nm.



	GS	CS
Pt – Pt	2.90 Å	2.68 Å
C _{ppy} – N _{NDI}	1.44 Å	1.43 Å
Dihedral Angle P _{ppy} – P _{NDI}	66.9°	61.6°

Figure S18. Primary structural differences between the optimized molecular geometries of ground-state (GS) and charge-separated (CS) state for complex **2**.

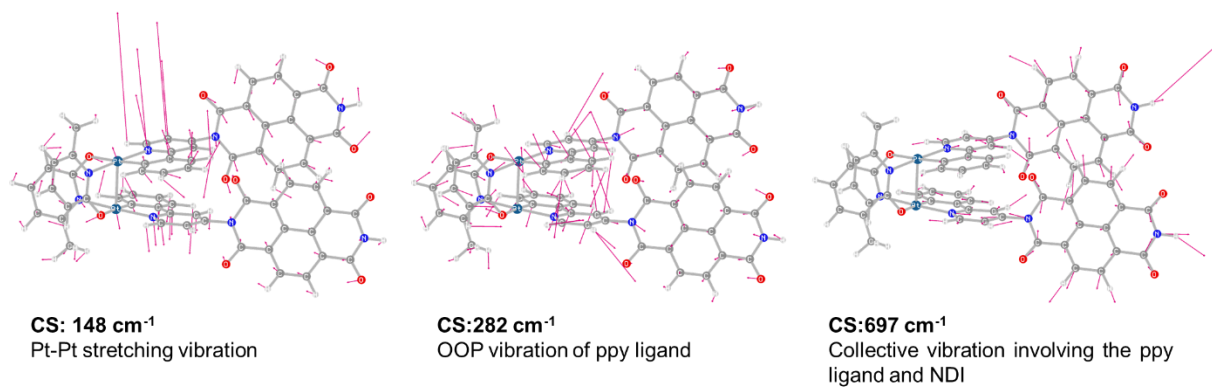


Figure S19. Calculated normal modes in the CS state for complex **2**, assigned to 150, 230 and 678 cm⁻¹ CWP motions.

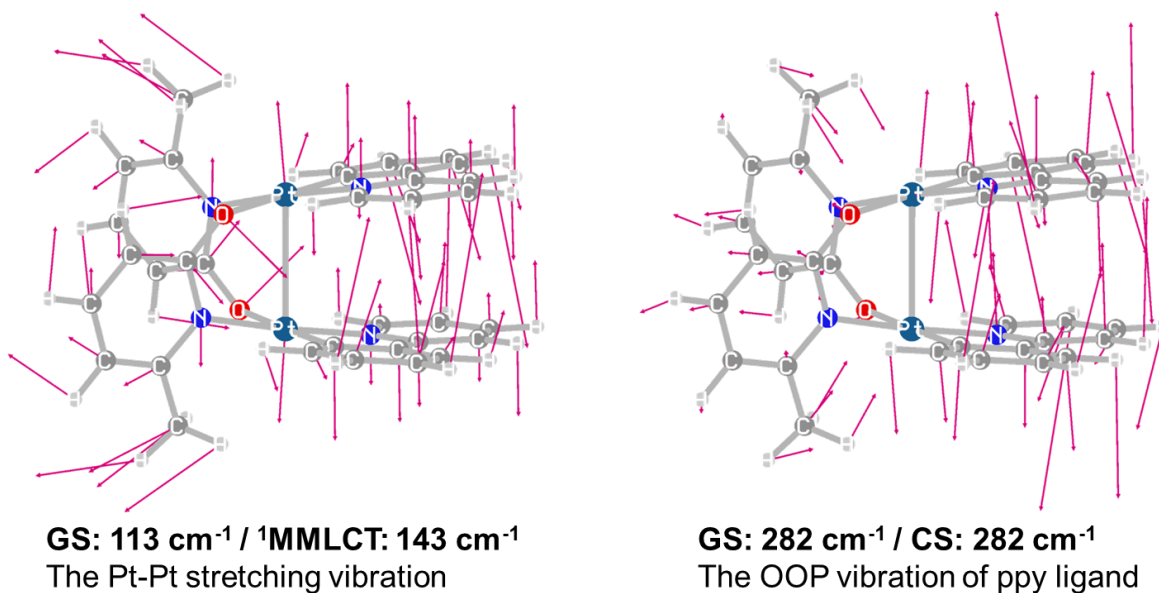


Figure S20. Calculated normal modes in the GS state for complex **1**, assigned to 150 and 230 cm⁻¹ CWP motions.

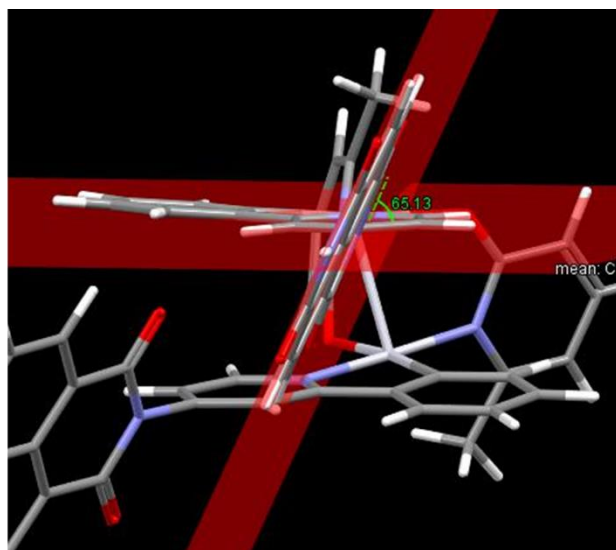
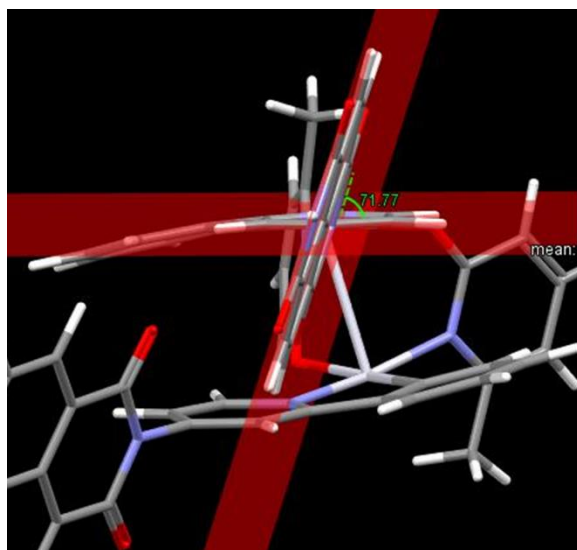


Figure S21. Calculated modulation of dihedral angle between the planes of ppy ligand and NDI during the Pt-Pt stretching vibrational motion (150 cm^{-1} CWP motion).

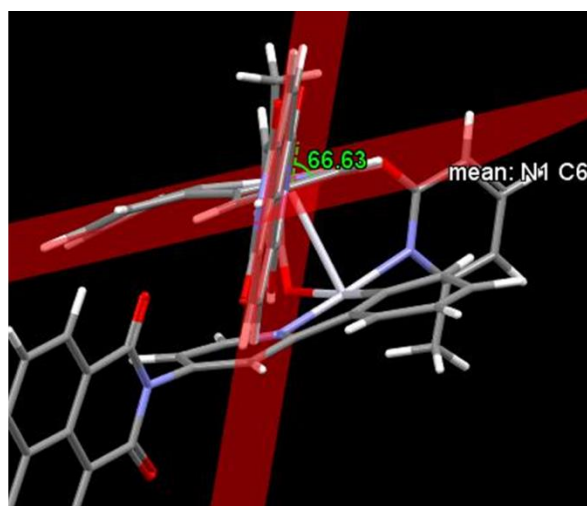
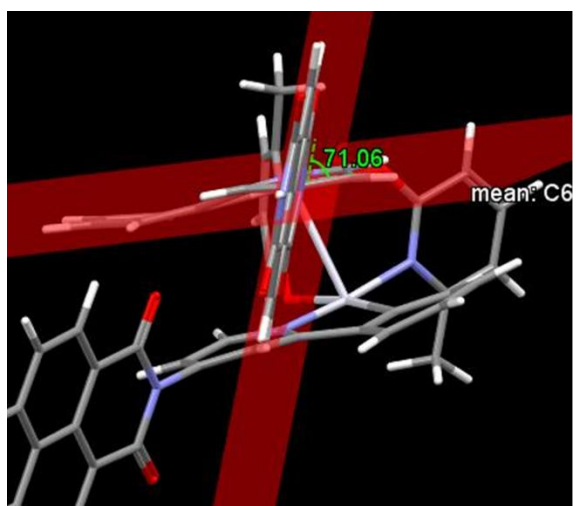


Figure S22. Calculated modulation of dihedral angle between the planes of ppy ligand and NDI during the OOP vibrational motions (230 cm^{-1} CWP motion).

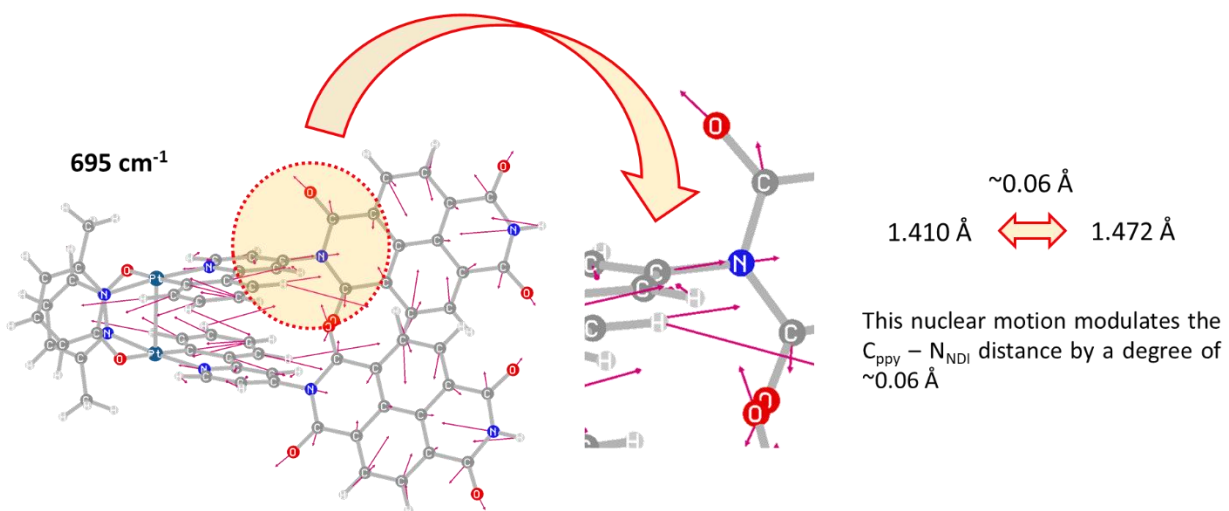


Figure S23. Calculated modulation of bond length between the ppy ligand and NDI in the GS state (678 cm^{-1} CWP motion).

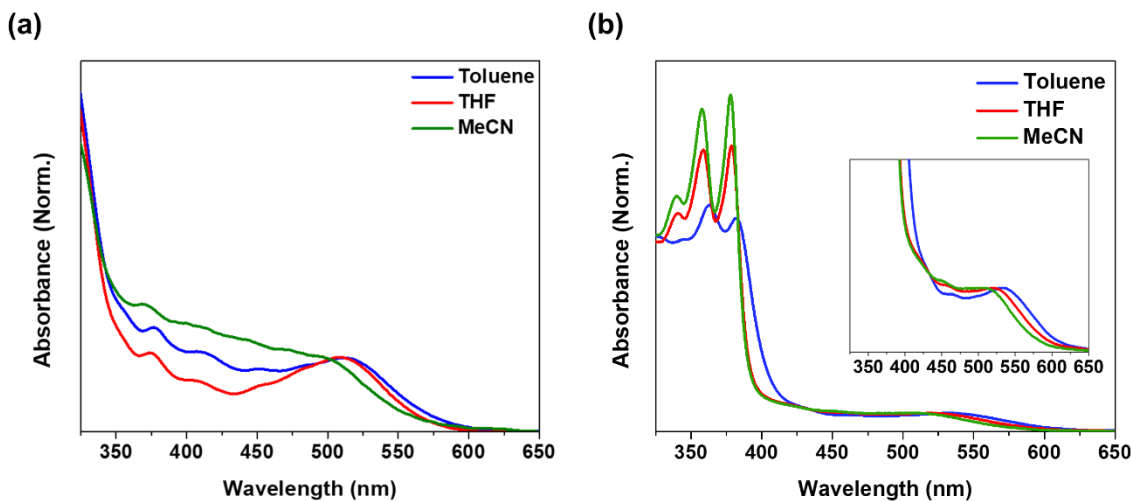


Figure S24. Steady-state absorption spectra of complexes **1** (a) and **2** (b) at toluene, THF and MeCN.

Solvent-polarity dependence in steady-state absorption measurements

The complexes **1** and **2** show a solvent-polarity dependence in their steady-state absorption spectra (Figure S24). Firstly, the MMLCT bands for **1** and **2** blueshift as the solvent polarity increase in the order of Toluene < THF < Acetonitrile (MeCN). The negative solvatochromism indicates that the ground-state is more polar than the excited-state, which has been also observed in the MLCT bands of mononuclear Pt(II) complexes.¹² Previously, transient direct current photoconductivity measurement identified that the excited-state dipole moment is reduced compared to the ground-state one, suggesting that the direction of the MLCT transition is opposite to the ground-state dipole vector.¹³ Since the orientations of MLCT and MMLCT transitions are to be same from Pt(II) metals to cyclometalating ligands, the negative solvatochromism observed in the MMLCT bands of **1** and **2** is also indicative of their polar ground-state. Secondly, the toluene solvent gives rise to significant changes in the NDI absorption accompanying a blueshift in the vibronic peaks of NDI electron acceptors and a growth in the I^{0-0}/I^{0-1} vibronic peak ratio. This feature indicates an increase in π - π interaction between the two NDIs. The interaction is enhanced in the nonpolar toluene solvent due to the hydrophobic alkyne chains of the NDIs which can induce the molecules to come together.

References

1. M. T. Vagnini, A. L. Smeigh, J. D. Blakemore, S. W. Eaton, N. D. Schley, F. D'Souza, R. H. Crabtree, G. W. Brudvig, D. T. Co and M. R. Wasielewski, *Proceedings of the National Academy of Sciences*, 2012, **109**, 15651-15656.
2. N. M. Shavaleev, E. S. Davies, H. Adams, J. Best and J. A. Weinstein, *Inorganic chemistry*, 2008, **47**, 1532-1547.
3. A. Chakraborty, J. C. Deaton, A. Haefele and F. N. Castellano, *Organometallics*, 2013, **32**, 3819-3829.
4. A. Chakraborty, J. E. Yarnell, R. D. Sommer, S. Roy and F. N. Castellano, *Inorganic Chemistry*, 2018, **57**, 1298-1310.
5. N. P. Weingartz, M. W. Mara, S. Roy, J. Hong, A. Chakraborty, S. E. Brown-Xu, B. T. Phelan, F. N. Castellano and L. X. Chen, *The Journal of Physical Chemistry A*, 2021, **125**, 8891-8898.
6. A. Grupp, A. Budweg, M. P. Fischer, J. Allerbeck, G. Soavi, A. Leitenstorfer and D. Brida, *Journal of Optics*, 2017, **20**, 014005.
7. M. J. Frisch, G. W. Trucks, H. B. Schlegel, G. E. Scuseria, M. A. Robb, J. R. Cheeseman, G. Scalmani, V. Barone, G. A. Petersson, H. Nakatsuji, X. Li, M. Caricato, A. V. Marenich, J. Bloino, B. G. Janesko, R. Gomperts, B. Mennucci, H. P. Hratchian, J. V. Ortiz, A. F. Izmaylov, J. L. Sonnenberg, Williams, F. Ding, F. Lipparini, F. Egidi, J. Goings, B. Peng, A. Petrone, T. Henderson, D. Ranasinghe, V. G. Zakrzewski, J. Gao, N. Rega, G. Zheng, W. Liang, M. Hada, M. Ehara, K. Toyota, R. Fukuda, J. Hasegawa, M. Ishida, T. Nakajima, Y. Honda, O. Kitao, H. Nakai, T. Vreven, K. Throssell, J. A. Montgomery Jr., J. E. Peralta, F. Ogliaro, M. J. Bearpark, J. J. Heyd, E. N. Brothers, K. N. Kudin, V. N. Staroverov, T. A. Keith, R. Kobayashi, J. Normand, K. Raghavachari, A. P. Rendell, J. C. Burant, S. S. Iyengar, J. Tomasi, M. Cossi, J. M. Millam, M. Klene, C. Adamo, R. Cammi, J. W. Ochterski, R. L. Martin, K. Morokuma, O. Farkas, J. B. Foresman and D. J. Fox, *Journal*, 2016.
8. P. J. Hay and W. R. Wadt, *The Journal of Chemical Physics*, 1985, **82**, 299-310.
9. A. J. Atkins, F. Talotta, L. Freitag, M. Boggio-Pasqua and L. González, *Journal of Chemical Theory and Computation*, 2017, **13**, 4123-4145.
10. J.-D. Chai and M. Head-Gordon, *Physical Chemistry Chemical Physics*, 2008, **10**, 6615-6620.
11. R. L. Martin, *The Journal of Chemical Physics*, 2003, **118**, 4775-4777.
12. F. N. Castellano, I. E. Pomestchenko, E. Shikhova, F. Hua, M. L. Muro and N. Rajapakse, *Coordination Chemistry Reviews*, 2006, **250**, 1819-1828.
13. F. W. M. Vanhelmont, R. C. Johnson and J. T. Hupp, *Inorganic Chemistry*, 2000, **39**, 1814-1816.